INL/EXT-17-42863

Light Water Reactor Sustainability Program

Effect of Swelling on Irradiation-Assisted Stress Corrosion Cracking

July 2017

U.S. Department of Energy

Office of Nuclear Energy

INL/EXT-17-42863

Effect of Swelling on Irradiation-Assisted Stress Corrosion Cracking

S. Teysseyre

July 2017

Prepared for the
U.S. Department of Energy
Office of Nuclear Energy

ABSTRACT

Type 304 stainless-steel material irradiated to 27 dpa in the Experimental Breeder Reactor II at Idaho National Laboratory was used to investigate the relation between void swelling, grain boundary cohesion, and intergranular crack growth rate (CGR) under solicitation by irradiation-assisted stress corrosion cracking.

The material selected offered two different swelling amounts (about 2 and 3.7%) in the same material at high dose. The entire material had been irradiated at the same time and under the same conditions; only the temperature gradient led to different swelling. This material, however, proved to be very resistant to irradiation-assisted stress corrosion cracking under pressurized water reactor conditions. The CGRs measured were very low, with the lowest CGR being obtained in the material exhibiting the most swelling. Micromechanical testing performed with the material exhibiting the higher crack propagation rate demonstrated that the irradiation damage (including void swelling) did not decrease grain boundary cohesion enough to make the grain boundaries the weak points under load. Crack path and crack tip analysis showed evidence of material modification ahead of the crack, but it is not clear at this point if the changes observed were caused by the crack advance or if their presence in front of the crack caused the low CGR measured.

CONTENTS

FIGURES

TABLES

ACRONYMS

AISI	American Iron and Steel Institute
BSE	back-scattered electron
CGR	crack growth rate
CRSS	critical resolved shear stress
CT	compact tension
EBSD	electron backscatter diffraction
IASCC	irradiation-assisted stress corrosion cracking
ICP-OES	inductively coupled plasma optical emission spectrometry
SEM	scanning electron microscopy
TEM	transmission electron microscopy
YS	yield strength

Study of the Effect of Swelling on Irradiation-Assisted Stress Corrosion Cracking

1. INTRODUCTION

To predict the susceptibility of high-fluence materials to irradiation-assisted stress corrosion cracking (IASCC), it is necessary to estimate how the features appearing at high fluence may affect IASCC. One of those features is void swelling. In a material with a voided microstructure, one can expect the high density of voids (both intergranular and intragranular) to affect the propagation of a stress corrosion crack. An intragranular void may affect local stress and deformation, and the presence of intergranular voids and bubbles may affect grain boundary cohesion and any diffusion process on the grain boundary. To study the effect of void swelling on IASCC crack propagation, this project tested a highly irradiated material whose irradiation conditions generated a swelling gradient through the component. The measurements of IASCC crack growth rates in 2 and 3.7% swelling, the analysis of the cracks generated, and the analysis of grain boundaries cohesion were used to estimate the role of swelling in IASCC.

2. EXPERIMENT PROCEDURES

2.1 Material

The material used in the study was cut from a thick hexagonal block made of American Iron and Steel Institute (AISI) 304 stainless-steel that served in one of the reflector assemblies in the Experimental Breeder Reactor II fast reactor at Idaho National Laboratory. The chemical composition was Fe-19.26Cr-8.81Ni-1.57Mn-0.43Si-0.056C-0.027P-0.03S wt%. The microstructure characterization of archive material suggests that 5% cold work was present at the center of the block prior to irradiation. The doses received and irradiation temperatures were evaluated from the temperature and dose calculated for the encasing duct using reactor physics and heat transfer calculation (Bond et al. 1999; Garner and Makenas 2006; Garner et al. 2007). This block was part of a series of five blocks that were in the reactor for 13 years: 4.5 years in Row 8 and 8.5 years in Row 16. However, 97% of the dose was received in Row 8. The material comes from Block 3, which was in the center of the core and received the highest dose (i.e., from 33 dpa for the face located toward the core center to about 22 dpa for the opposite face). As the specimens were retrieved toward the center of the block, the dose received was about 27 dpa. More specifically, the material comes from a 0.5-in.-thick coin labelled 3F3 that was initially located toward the center of Block 3 (Figure 1). The time-averaged temperature was 390°C; however, due to gradient gamma heating, there was an off-center peak in temperature inside the block (Figure 2). The maximum average temperature inside Block 3 was estimated to be about 460°C (Garner et al. 2014). This temperature gradient is expected to have led to a swelling gradient. Ultrasonic time-of-flight measurements performed on Coin 3F3 confirmed an off-center swelling peak, with a maximum at about 3.7% swelling and a minimum of less than 2% (Garner et al. 2013; Garner et al. 2014).

2.2 Specimens

Two pairs of compact tension (0.25T CT) specimens were machined. The location for machining was determined such that, for each pair of CT specimens, the cracks would grow in a material with similar swelling. Two specimens were machined so the cracks would grow in a material with 3.7% swelling, and two specimens were machined so cracks would grow in less than 2% swelling. The percent of swelling used was an estimation that was determined by ultrasonic technique. The orientation of the CTs with regard to the component was the same. Details regarding the machining steps can be found in Teysseyre (2015). The first specimens to be tested were CT1 and CT2. Their locations in the coin is shown in Figure 3. The specimens' dose rates were respectively 160 and 180 mR/hour at 30 cm.

For this project, it was decided that short leads would be connected to the specimens as part of the specimen machining. The small leads were placed so their connections to the direct current potential drop leads in the autoclave were performed without moving the specimen. A photograph of the CT1 specimen with the leads attached is presented in Figure 4.

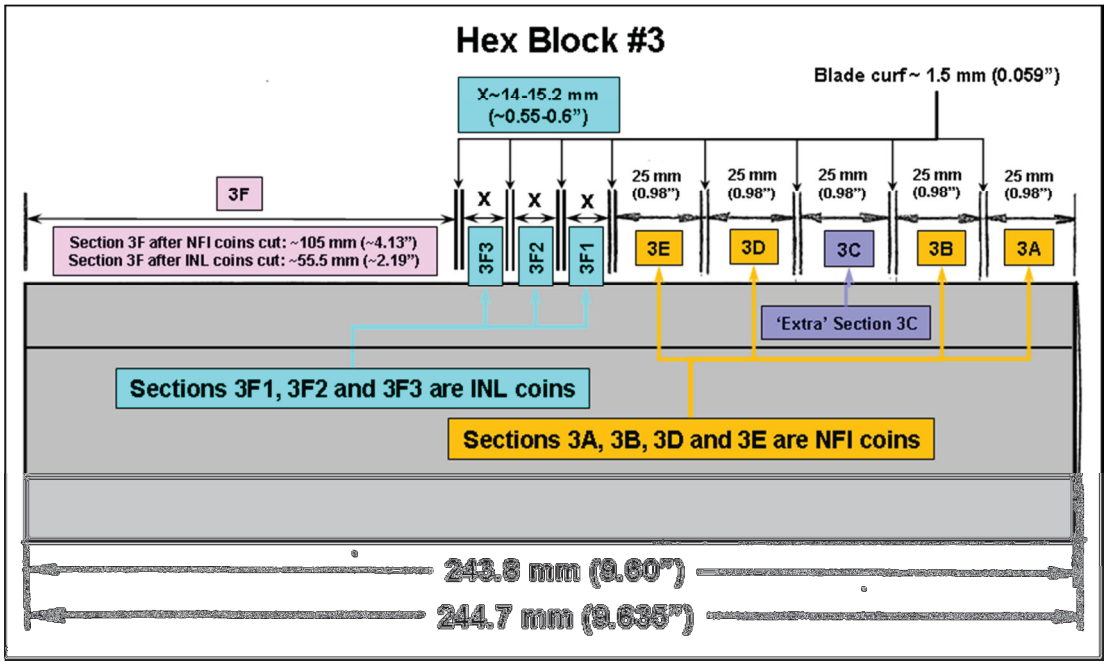

Figure 1. Schematic of Block 3 from which the material used for this study (Coin 3F3) was cut.

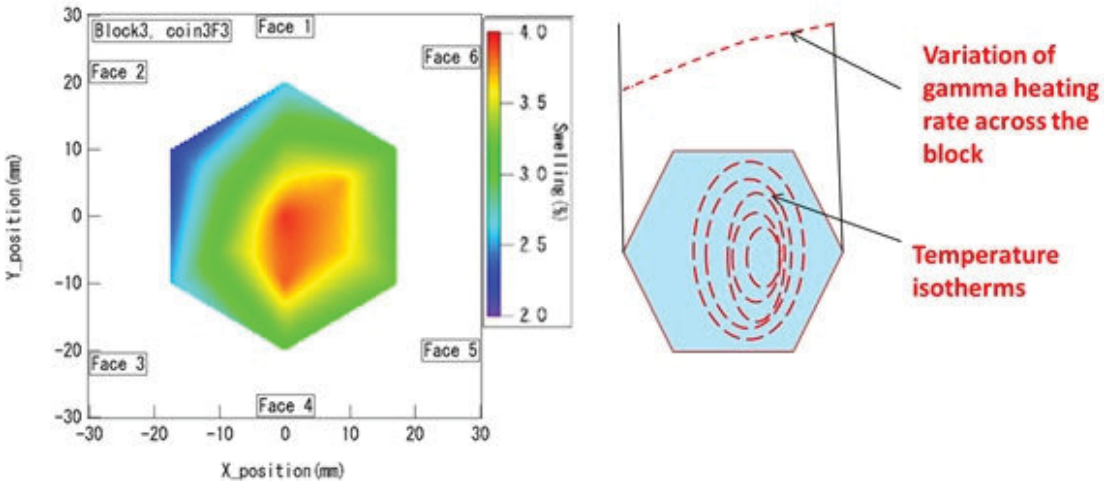

Figure 2. Temperature distribution across the block (Garner 2014 et al.).

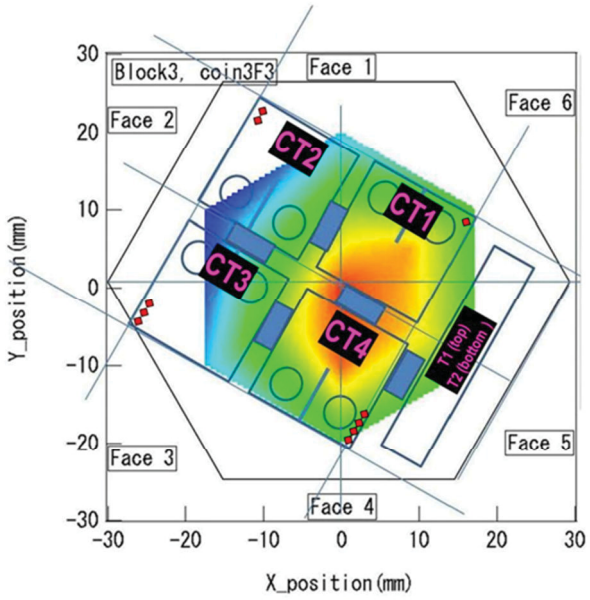

Figure 3. Locations and orientations of the four CT specimens (CT1, CT2, CT3, and CT4) as they were cut in the hexagonal coin. T1 and T2 show the locations of the tensile specimens.

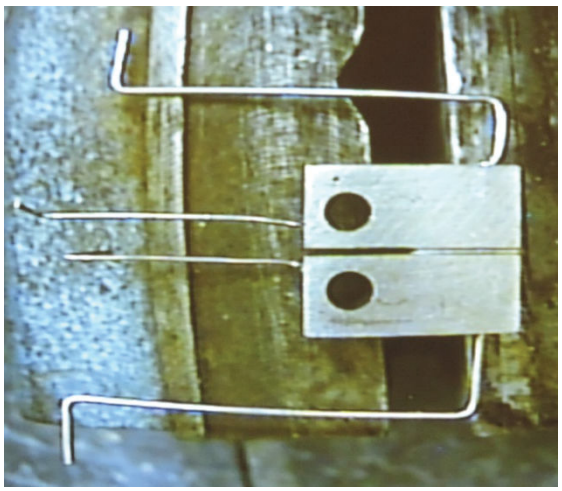

Figure 4. CT1 specimen after short current and potential lead welding was completed. Dimensions of the photograph may appear distorted, because the photograph was taken from a video monitor of the specimens.

2.3 Irradiation-Assisted Stress Corrosion Cracking Experiments

The IASCC experiments were performed in a shielded testing loop. The water was continuously refreshed with a flow rate of about 200 mL/minute for a 4-L autoclave; the water chemistry was continuously monitored and controlled. The dissolved gas concentration was controlled by applying an overpressure of pure hydrogen at room temperature before water flowed into the high-pressure, high-temperature part of the loop. The ion content in the water was controlled by flowing water through an ion exchanger to remove corrosion products. The tests were performed in a pressurized water reactor environment, meaning pure water with 1,000 ppm of boron and 2 ppm of lithium added and 25 cc/kg of dissolved hydrogen. Water chemistry was controlled by measuring water conductivity and pH. During the experiment, water chemistry was verified using inductively coupled plasma optical emission spectrometry

(ICP-OES). AT5 software provided by the GE Global Research Center was used to monitor crack growth and control load. Crack length was monitored using the direct current potential drop technique. Details regarding shielding, loading procedures, and water chemistry control are provided in Appendix A.

2.4 Post-Test Characterization

Once an experiment was completed, a slice of the specimen tested was retrieved and polished in order to proceed to analysis of crack propagation path and analysis of the crack by scanning and transmission electron microscopy. Some of the retrieved material was used to perform micromechanical tensile testing with this material.

2.4.1 Post-Test Specimen Slicing

Upon completion of the crack growth rate (CGR) test, the specimen was removed and placed in a specially designed jig (Figure 5) that was connected to a low-speed saw located in a glovebox. This jig allowed slicing of the specimens, as illustrated in Figure 5, with minimum exposure to the operator and high repeatability.

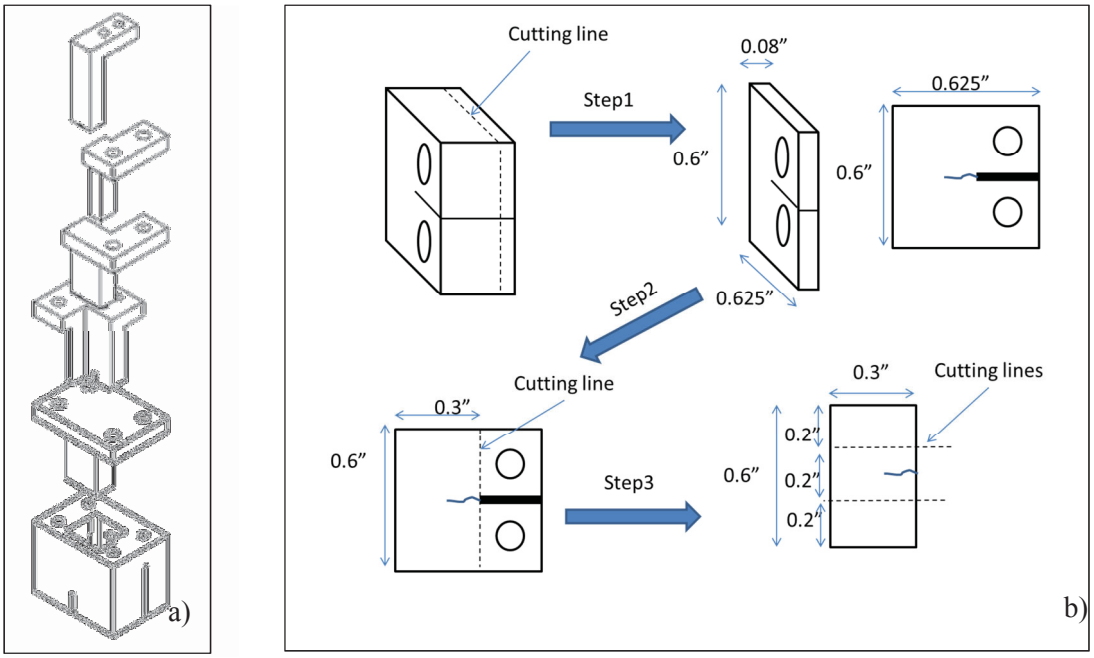

Figure 5. Schematic of the jig used to slice the 0.25T-CT specimen in the glovebox (a) and the various steps taken to slice the specimen to prepare it for post-test characterization.

2.4.2 Procedure for Single Grain Boundary Testing

Specimens (2 mm × 2 mm × 0.5 mm) were extracted from the CT specimens, polished to the quality required to permit electron backscatter diffraction (EBSD), and shipped to the University of California-Berkeley Nuclear Materials Laboratory. The material was used to manufacture tensile bars for micromechanical testing. The equipment used included the dual focused-ion beam Quanta 3D FEG, which incorporated GIS (Pt) energy dispersive spectroscopy/EBSD (Oxford), scanning transmission electron microscopy detector, Kleindick manipulators, and a Hysitron PI85. Rough milling was conducted at 30 keV with currents of 1 to 3 nA, and the final cleaning was performed at 0.3 nA.

EBSD was used to map the grain and grain orientations of selected regions prior to sample fabrication, which allowed the tensile bars to be located within a single grain or allowed the selection of specific grain boundaries and the determination of the Schmid factor of each grain along the axis of the

tensile bars. Tensile bar selection and determination of its orientation is illustrated Figure 6. Once selected, the area of interest was removed, as illustrated in Figure 7, the orientation of the grain boundary and surrounding material was completed.

During completion of the tensile test, a stress-strain curve was generated. The yield strengths (YSs) from different grains cannot be compared, so the critical resolved shear stress (CRSS) was used for comparison among different grains.

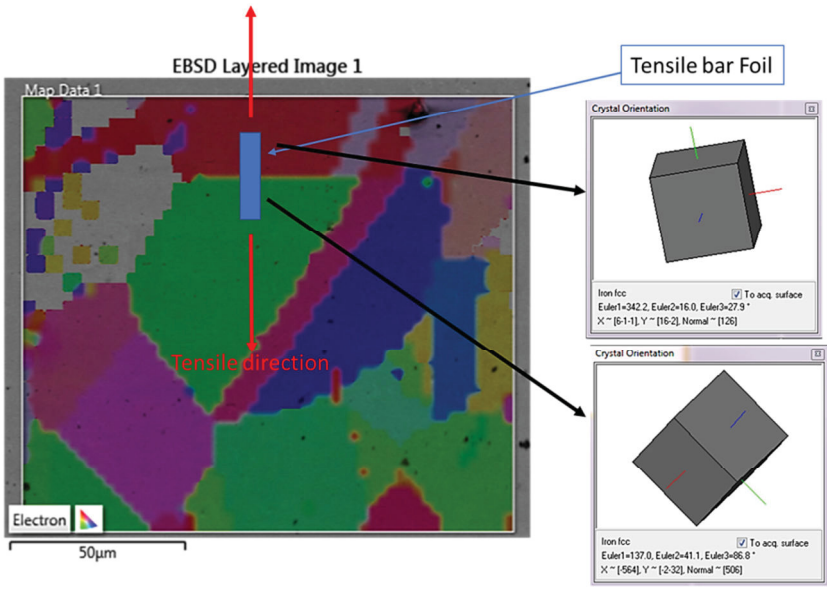

Figure 6. Illustration of the selection and indexing of grain boundary for micromechanical testing.

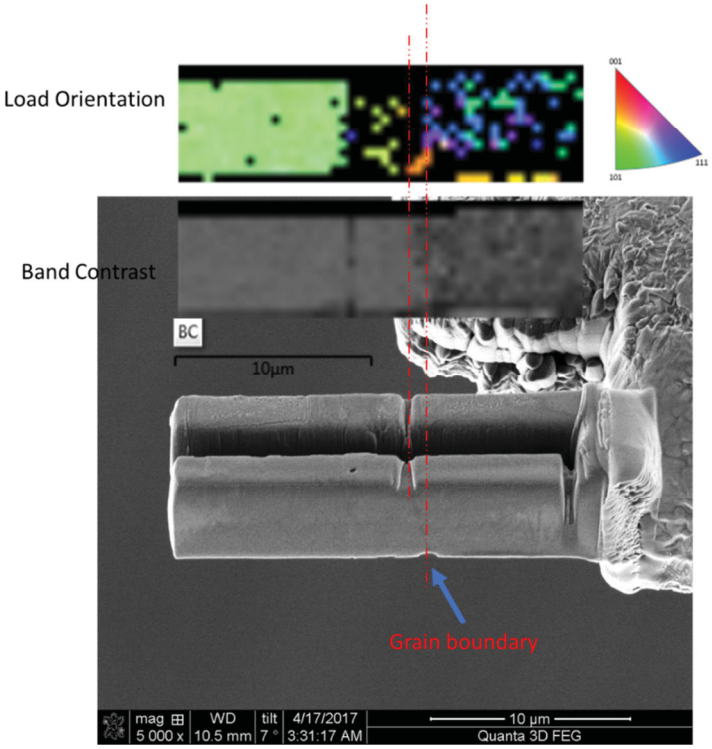

Figure 7. Preparation of a tensile bar for micromechanical testing.

3. RESULTS:

3.1 Effect of Swelling on Crack Growth Rates

The IASCC CGRs were determined for 2 and 3.7% swelling material from 0.25T CT specimens in a pressurized water reactor environment (325°C, 1,000 ppm boron, 2 ppm lithium, 25 cc/kg dissolved hydrogen). The specimen containing material with 2% swelling was tested at a nominal applied K level of 16 ksi√in. After several days in the environment to ensure stabilization of the corrosion potential, the specimen was fatigue pre-cracked at a maximum applied K of 14 ksi√in. and a loading ratio of 0.3 at a frequency of 0.5 Hz. In the following pre-cracking steps, the applied K was increased to the target test K (16 ksi√in.) as R was increased and holding time under load was applied. Table 1 summarizes the various steps used. The specimen responded well to each loading change with a stable crack propagation rate at each step (Figure 8). At about 630 hours, a long power outage caused a controlled interruption of the experiment. The experiment was restarted, and several steps were introduced to verify that the specimen was still responding to the solicitation. Loading was then transitioned to constant K (Figure 9). The CGR measured at constant K=16 ksi√in. is 1.9×10^{-9} mm/s (or 1.9×10^{-12} m/s). The applied K was then increased to 18 ksi√in. under this condition. The CGR stabilized at 4.6×10^{-9} mm/s (Figure 10).

Table 1. CGR measured for each loading condition for specimen CT2 (<2% swelling).

Steps	Planned Starting (a/W)	Hours	K_{max}	R	Frequency, Hz	Hold Time (seconds)	CGR (mm/s)
1	0.400	501	14	0.3	0.5	0	
2	0.430	529.9	15	0.4	0.5	0	1.66×10^{-5}
3	0.440	531.99	16	0.6	0.2	0	4.8×10^{-6}
4	0.450	539	16	0.6	0.05	0	1.63× 10-^{6}
5	0.460	560.7	16	0.6	0.01	9,000	5.26×10^{-7}
6	0.470	628.9	16	0.6	0.001	9,000	9.96×10^{-8}
Program interruption at a/w = 0.47038; specimen was unloaded to 200 lb. Program restarted for a/w = 0.470000, K16, R0.6, F0.001, H9000.							
7	0.470	0	16	0.6	0.001	9,000	1.36×10^{-8}
8	0.47105	120	16	0.6	0.01	0	6.25×10^{-7}
9	0.47508	144	16		0.001	9,000	2.6×10^{-8}
10	0.47540	169	16	0.6	0.01	9,000	1.14×10^{-8}
11	0.47549	190	16	0.6	0.01	0	5.41×10^{-7}
12	0.47806	208	16	0.6	0.01	9,000	1.18×10^{-8}
13	0.47920	501	16	0.6	0.001	9,000	1.27×10^{-8}
14	0.47958	605	16	1			1.91×10^{-9}
15	0.47973	1,600	16 to 18	0.6	0.001	9,000	
16			18	1			4.6×10^{-9}

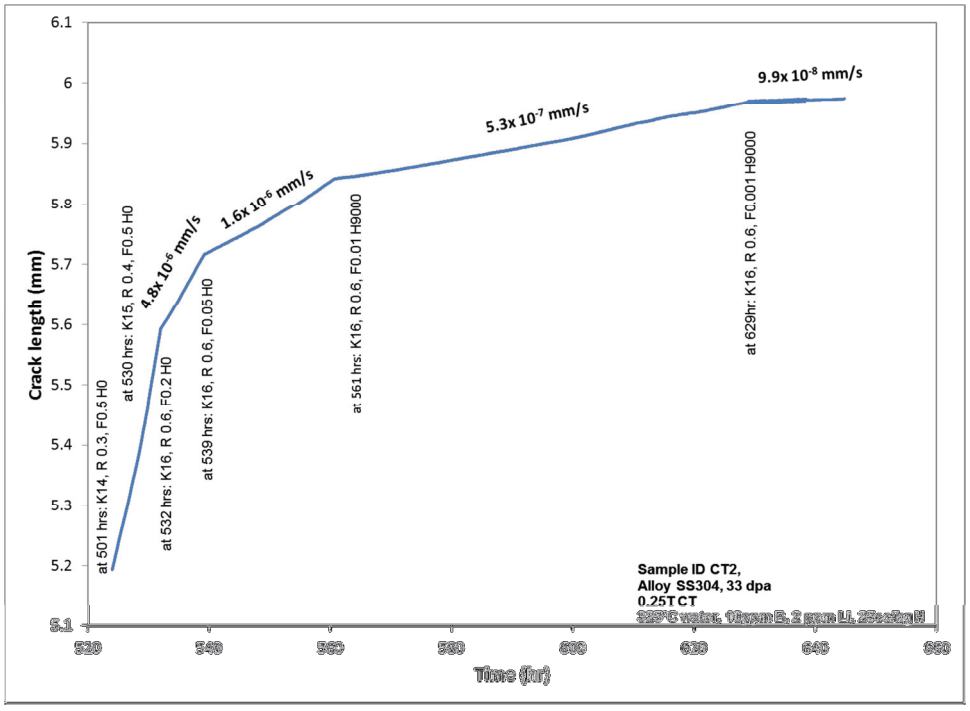

Figure 8. Initiation of the experiment, fatigue pre-crack.

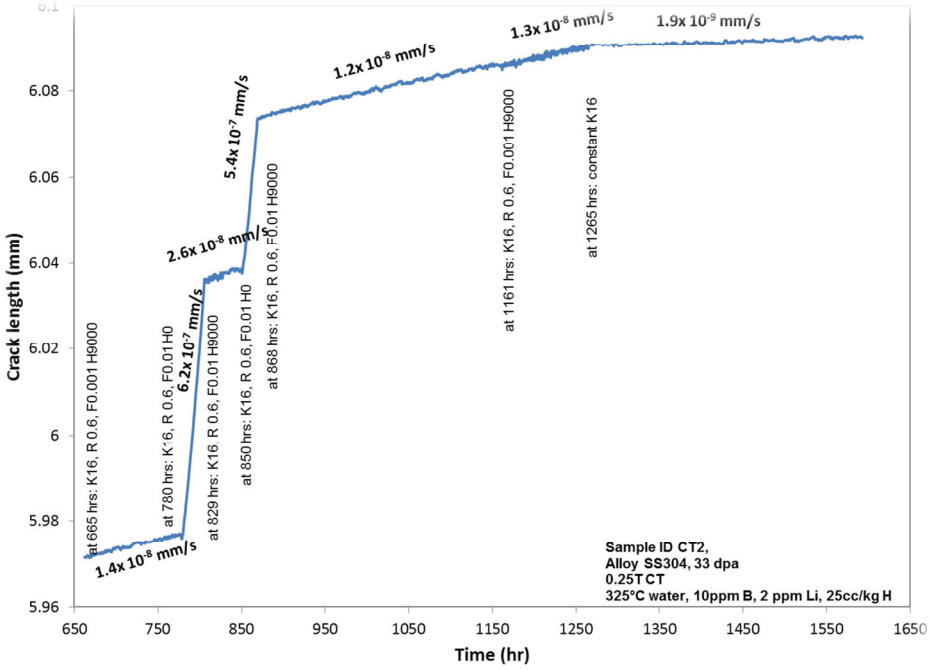

Figure 9. Second part of the experiment after restart, pre-cracking, and transition to constant K.

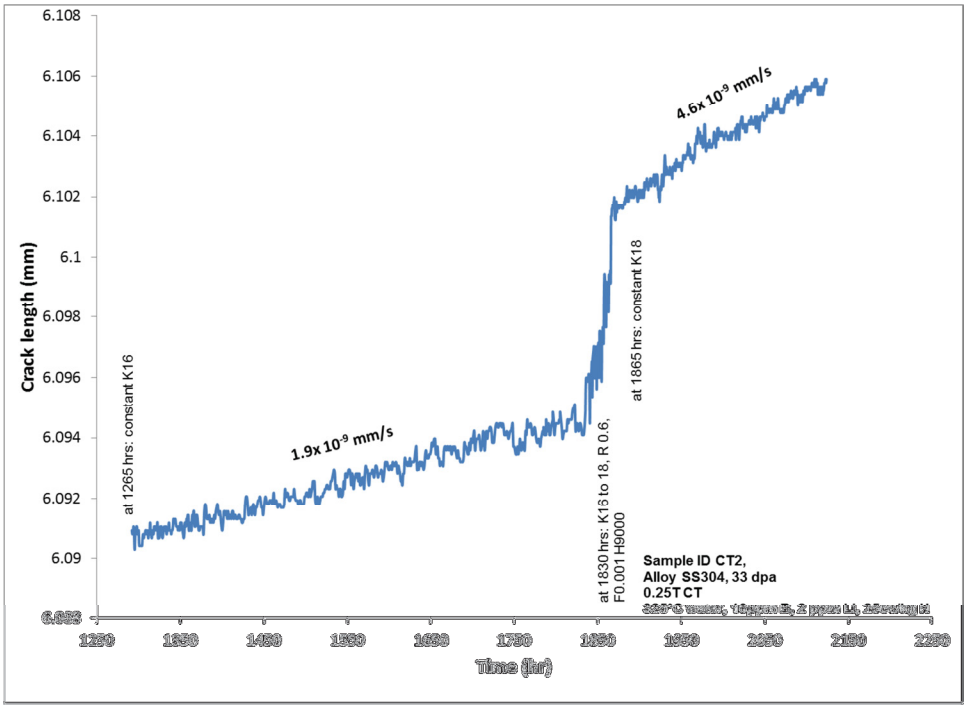

Figure 10. Crack length versus time for the 2% swelling specimen at applied K=16 ksi√in. and 18 ksi√in.

The specimen containing 3.7% swelling was tested with the same approach at three different applied K: 16 ksi√in., 18 ksi√in., and 20 ksi√in. The evolution of crack length as a function of time is presented in Figures 11 through 13. Table 2 summarizes the different steps and associated CGRs. The CGR measured at applied K=16 ksi√in. was 3.5×10^{-10} mm/s to be compared with the 1.9×10^{-9} mm/s measured at 2% swelling. At applied K=18 ksi√in., the CGR increased to 9.9×10^{-10} mm/s to be compared with the 4.6×10^{-9} mm/s. When loading increased to applied K=20 ksi√in., the crack responded with a higher CGR (2.17×10^{-9} mm/s), which was still very low.

From information collected from NUREG/CR-7027, the CGR measured was about 1 order of magnitude below most of the data and the NUREG-0313 curve (which is about 1×10^{-10} m/s at K=16 ksi√in) (Figure 14). Despite the low CGR, it appears that higher swelling did not lead to a higher CGR.

3.2 Imaging of Voids Distribution

Back-scattered electron (BSE) imaging allowed the imaging of the voids on a large area (Figure 15). Scanning the specimens away from the cracked areas permitted researchers to determine that the voids were distributed more within the grains than intergranularly (Figure 16a), with some evidence of a void denuded zone. Some grain boundaries exhibited denuded zones that may be related to local phase transformation (Figure 16b).

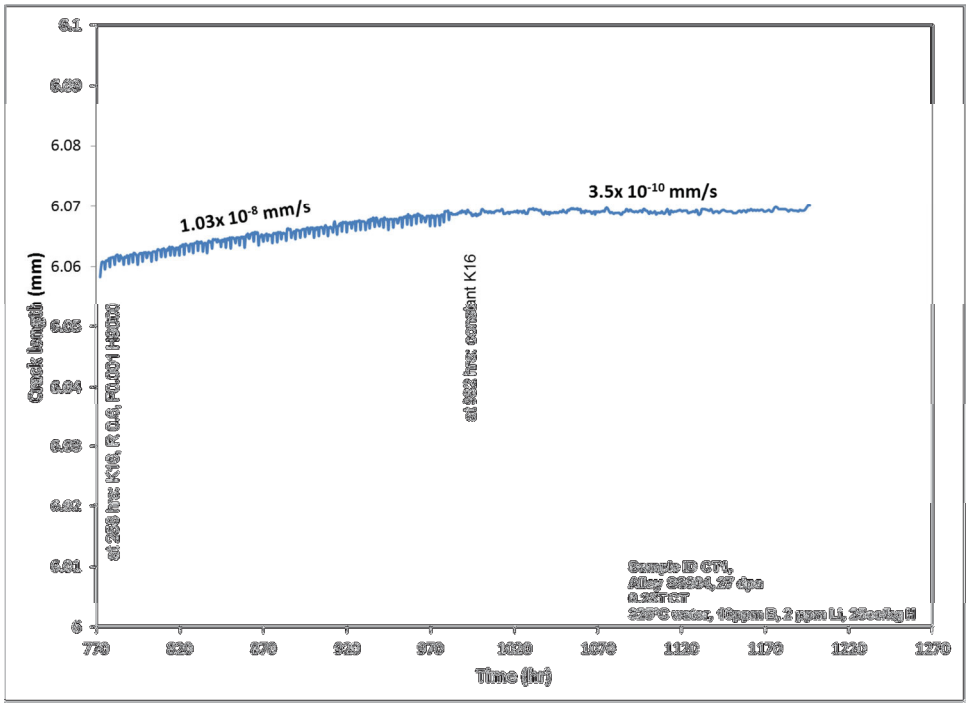

Figure 11. Crack length versus time for the 3.7 swelling specimen at applied K=16 ksi√in.

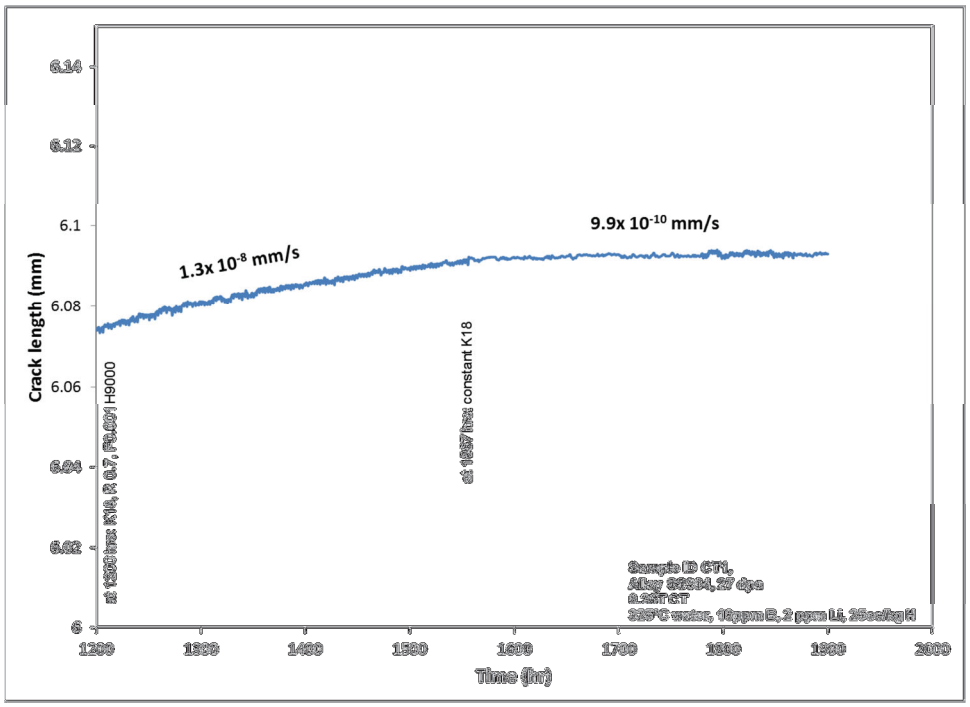

Figure 12. Crack length versus time for the 3.7% swelling specimen at applied K=18 ksi√in.

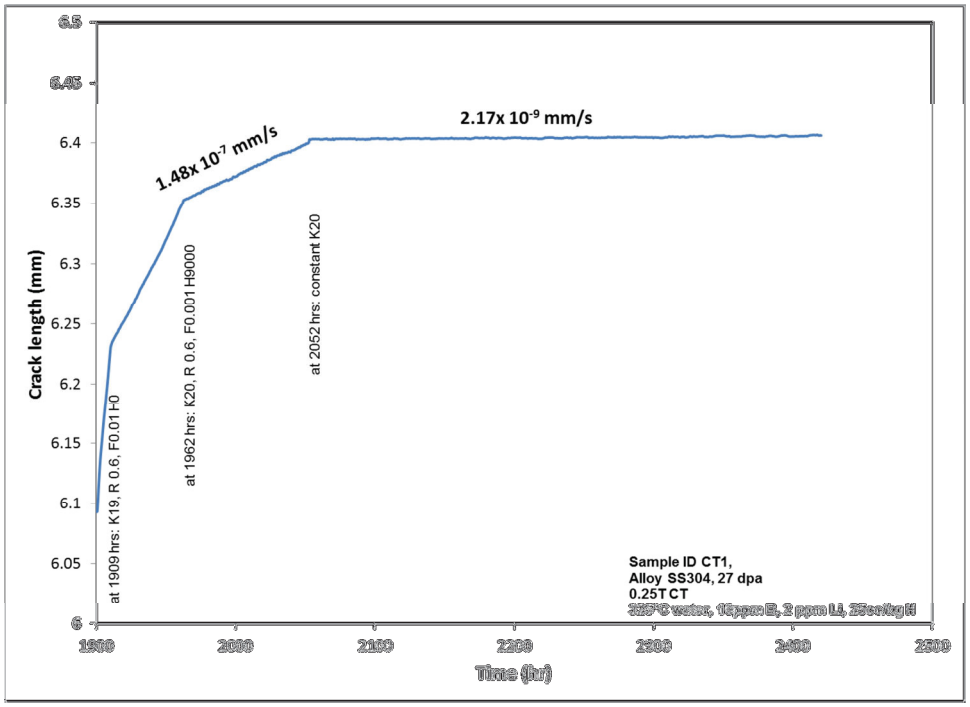

Figure 13. Crack length versus time for the 3.7% swelling specimen at applied K=20 ksi√in.

Table 2. CGR measured for each loading condition for specimen CT1 (3.7% swelling).

Steps	Planned Starting (a/W)	Hours	K_{max}	R	Frequency (Hz)	Hold Time (seconds)	CGR (mm/s)
1	0.400	0	15	0.4	0.5	0	
2	0.430	0	15	0.4	0.5	0	1.18×10^{-5}
3	0.440	162	16	0.6	0.2	0	4.02×10^{-6}
4	0.450	168.2	16	0.6	0.05	0	1.48×10^{-6}
5	0.460	190.6	16	0.6	0.01	9,000	5.1×10^{-7}
6	0.470	257.9	16	0.6	0.001	9,000	1.03×10^{-8}
7	0.47786	982.2	16	1	0		3.5×10^{-10}
Power loss; specimen was unloaded to 50 lb. + tare.							
8	0.47868	1200.7	18	0.7	0.001	9,000	1.3×10^{-8}
9	0.47968	1557.1	18	1			9.9×10^{-10}
10	0.48343	1900.3	18–20				1.48×10^{-8}
11	0.0.50416	2052.5	20	1			2.17×10^{-9}

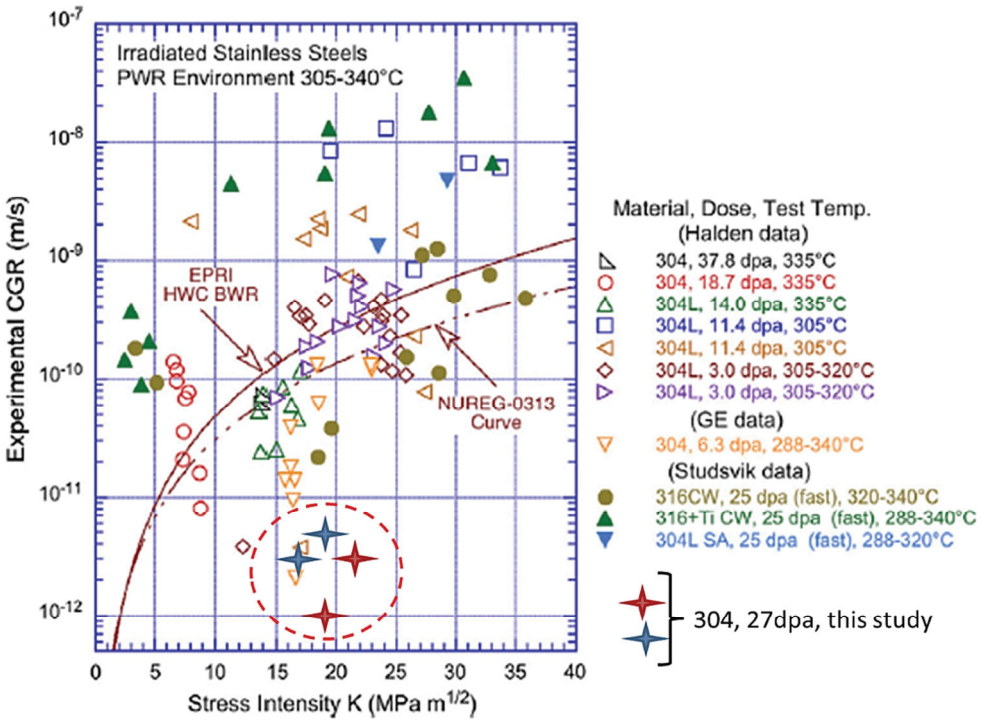

Figure 14. CGR generated in this study compared to the literature (Chopra and Roa 2011).

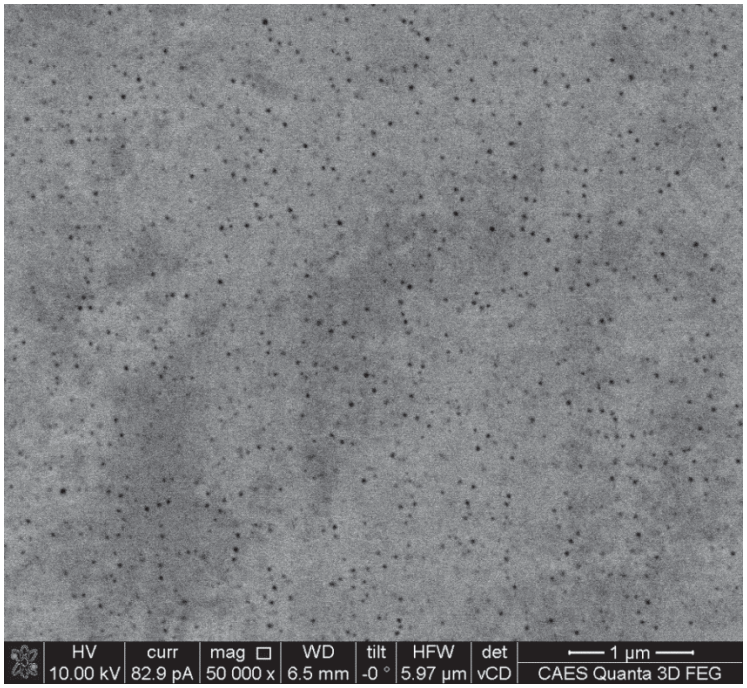

Figure 15. Imaging of voids in the material using BSE imaging.

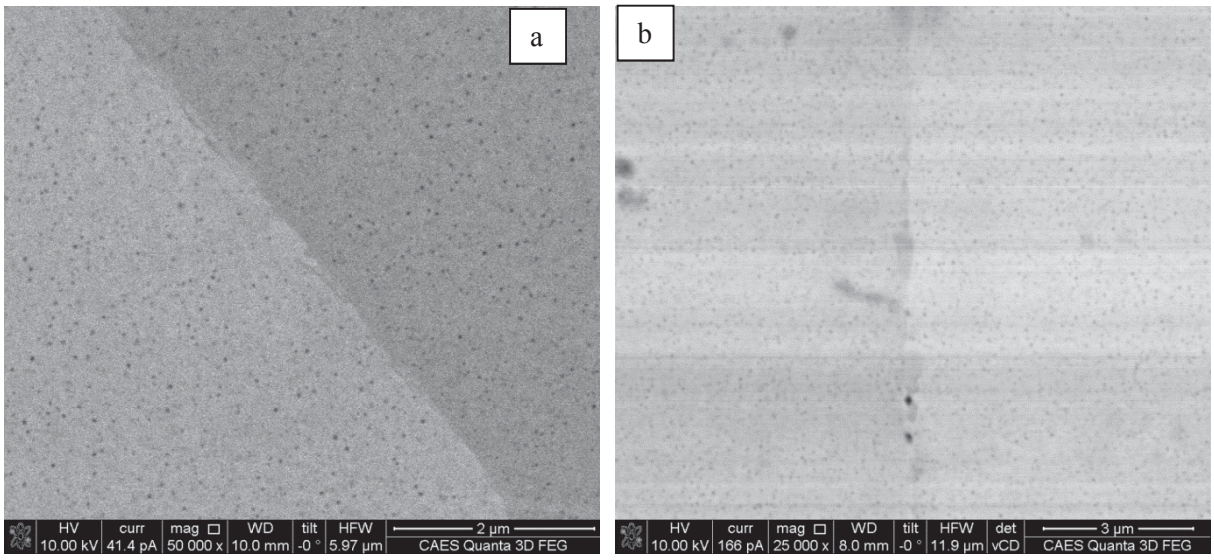

Figure 16. BSE imaging of areas containing grain boundaries.

3.3 Crack Path and Crack Tip Analysis

The specimens were cross sectioned to allow the visualization of cracks. Scanning electron microscopy (SEM) and EBSD analyses confirmed the transgranular nature of the crack during the fatigue and transition to stress corrosion cracking steps and the intergranular nature of the crack during the stress corrosion cracking step. The entire cracked area was scanned. Figure 17 shows the area corresponding to the last part of the test performed with the 2% swelling specimen, which is the area where the IASCC CGRs were determined. On this two-dimensional representation, the crack was drawn above the EBSD map. One can see that the crack is branching to go around a grain that is in the path of the crack. The grain reference misorientation deviation analysis during the prefatigue steps (Figure 18a) and during the IASCC steps (Figure 18b) shows the presence of strain along the crack. It was not localized along the crack walls only, but pockets can be seen at localized areas in a band of about 200 µm wide along the crack. Of interest is an evident strain localized along the grain boundary in front of the deepest crack.

SEM analysis indicated that the main crack tip (tip Number 1 corresponding to the deepest crack) seemed blunted (Figure 19b), with a large area corroded more like crevice pitting than stress corrosion cracking. In this cross section, it appears that the grain boundary located in front of the crack was a low-angle boundary that was not very susceptible to cracking. Note that strain was accumulating along this grain boundary (Figure 18b). The BSE imaging in front of this blunted crack does not reveal any particular cavity distribution. Two other side cracks, Cracks 2 and 3 as noted in Figure 19c, exhibited features that may indicate that those cracks were the active cracks during the last part of the test. However, it must be stated that such analysis was performed on a cross section, which is a two-dimensional snapshot of a phenomenon occurring in three dimensions. It is possible that the random sampling led the researchers to observe the main crack in an area where propagation was difficult, but that the observation would be different a couple of grain sizes away from this area.

The two secondary cracks exhibited interesting features ahead of the crack tip (Figure19c). Both have phases along the grain boundary that seem denuded from voids (Figures 20 and 21). In front of Crack 2, beyond those phases appeared a series of voids along the grain boundaries. Such accumulation of voids ahead of the crack could be a precursor to cracking, but it is unclear if such accumulation was a consequence of the stress corrosion cracking test or if it was present in the material previously.

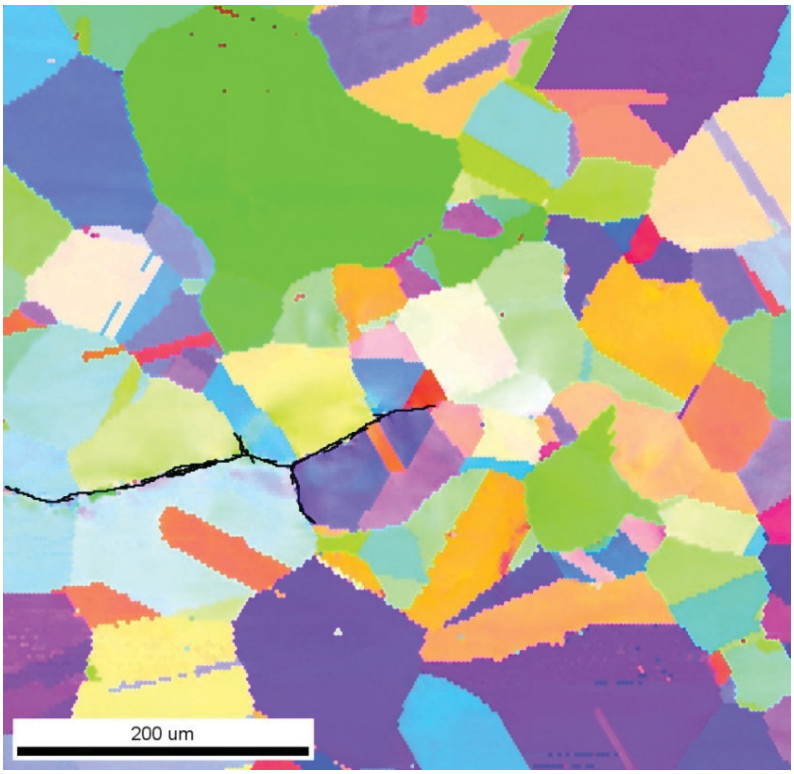

Figure 17. EBSD map and crack path during IASCC test for the 2% swelling specimen

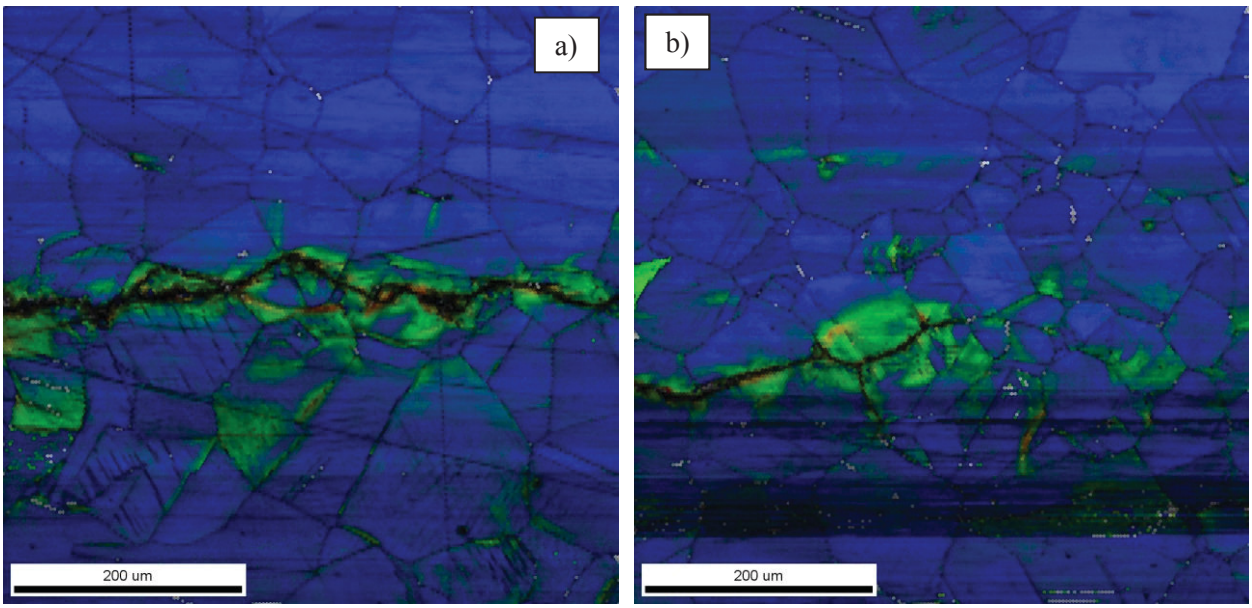

Figure 18. Grain reference misorientation deviation on crack path during fatigue (a) and IASCC test (b) for the 2% swelling specimen.

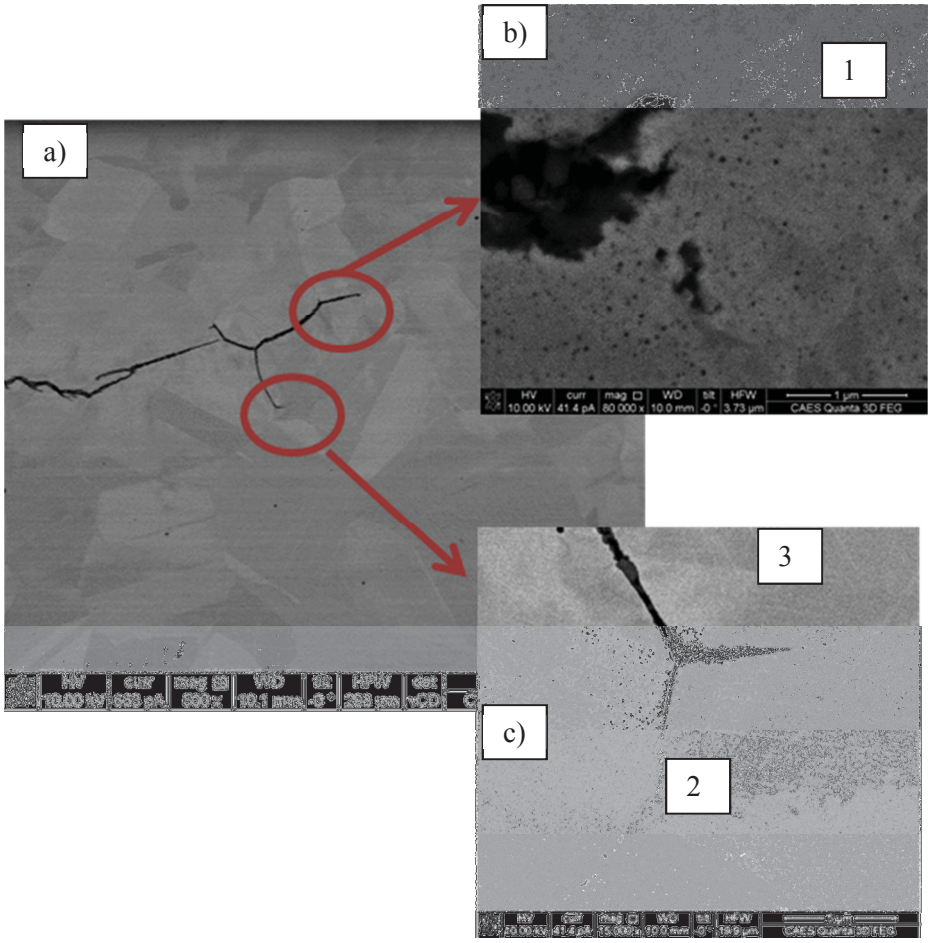

Figure 19. SEM imaging of the cracks located in the 2% swelling specimen.

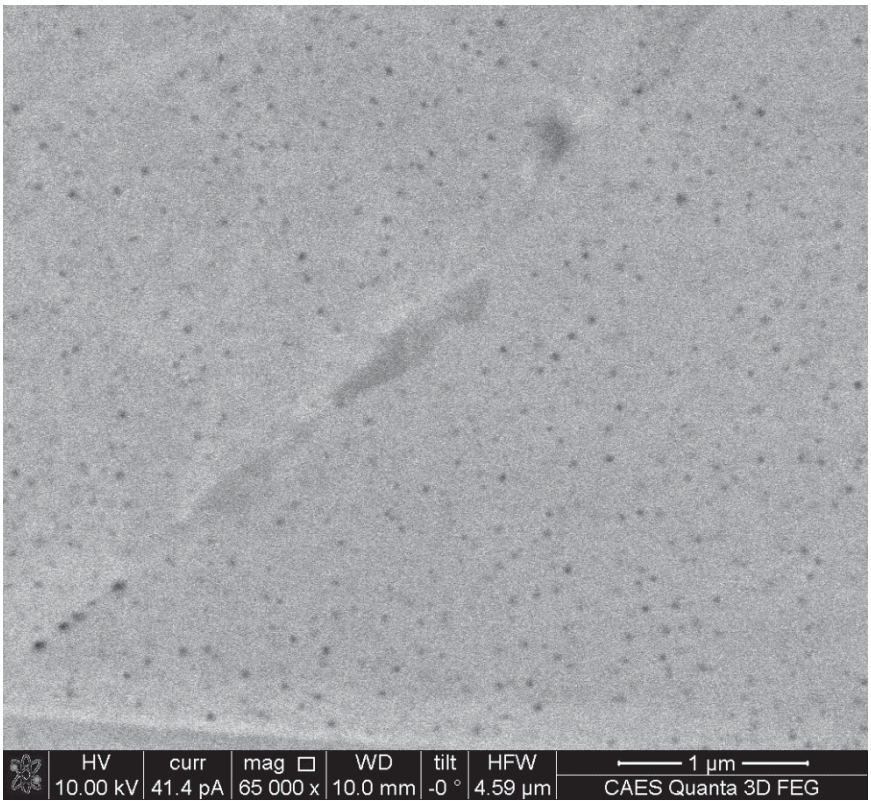

Figure 20. BSE imaging of the Crack 2 from the 2% swelling specimen.

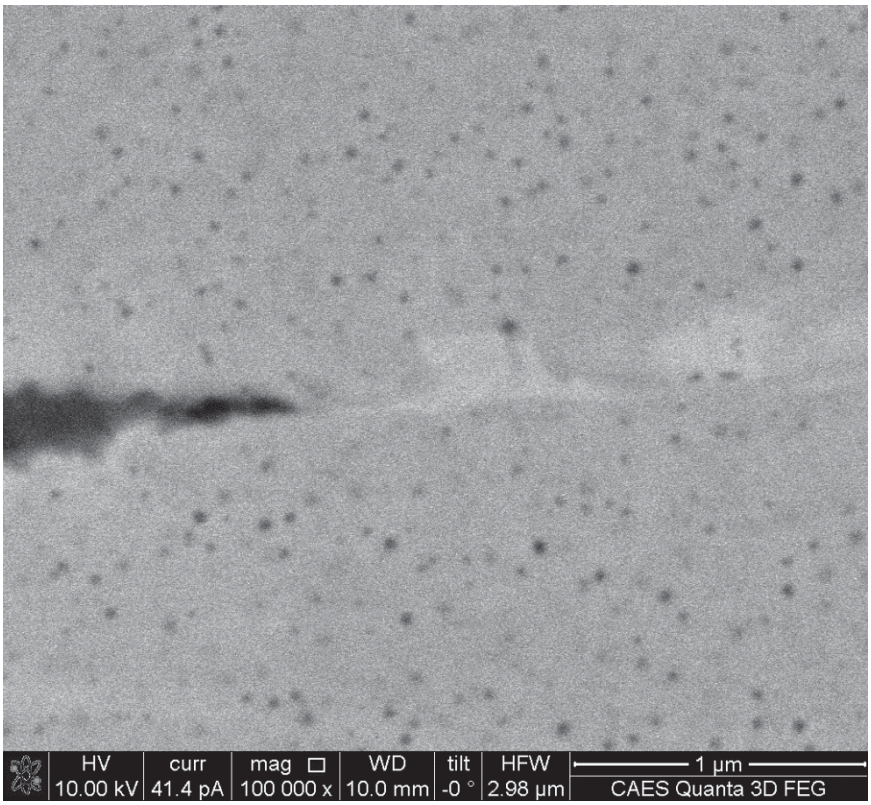

Figure 21. BSE imaging of the Crack 3 from the 2% swelling specimen.

Focused-ion beam lift-out was performed to remove the crack tips and conduct transmission electron microscopy (TEM) analyses (Figure 22). The analysis of Crack 2 indicated that the crack tip was not as narrow as expected and that a pocket of corrosion products was present ahead of the crack (Figure 23). The corrosion products along the crack were mainly Fe-Ni-O, and the larger pocket of corrosion product was mainly composed of Fe-Cr-O. Ahead of this corrosion pocket was a 200-nm band that was composed of two layers with different phases (alpha and gamma) and two slightly different chemical compositions (19.7-Cr, 6.6-Ni, Fe and 12.9Cr, 4.6Ni, Fe) (Figure 24). Further the diffraction analysis (Figure 25) showed that the band was composed of both alpha and gamma phases.

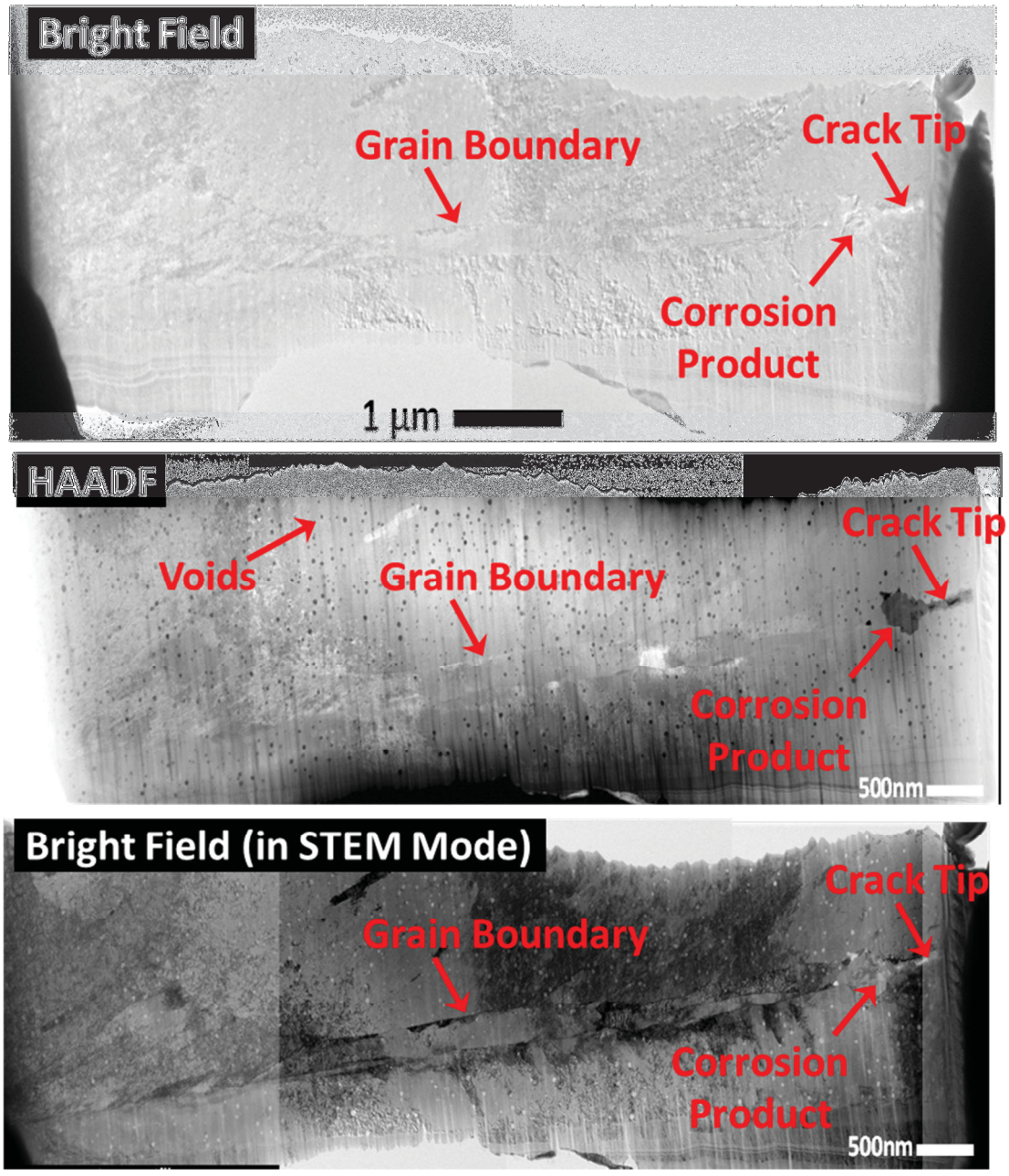

Figure 22. TEM imaging of Crack 2 from the 2% swelling specimen.

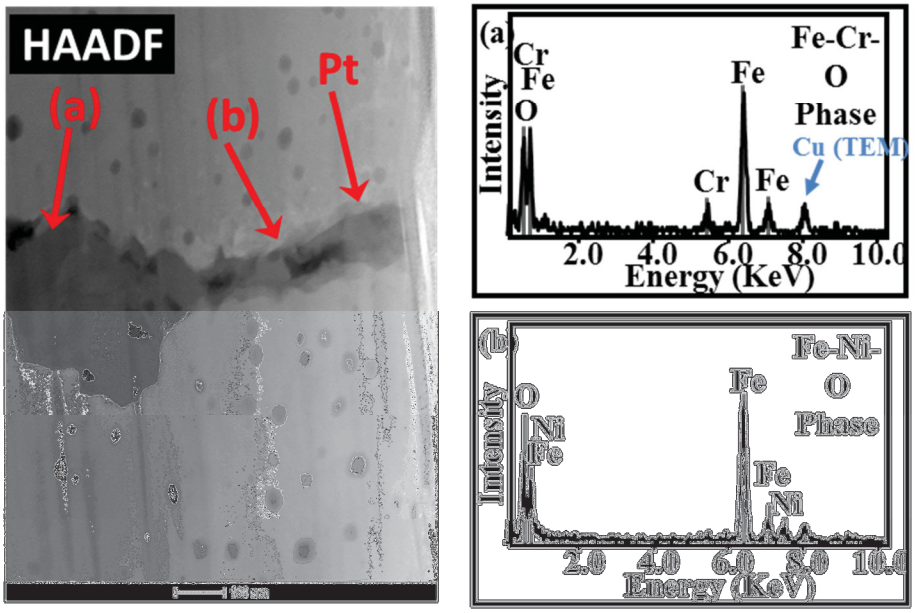

Figure 23. Actual crack tip and corroded area of Crack 2 from the 2% swelling specimen.

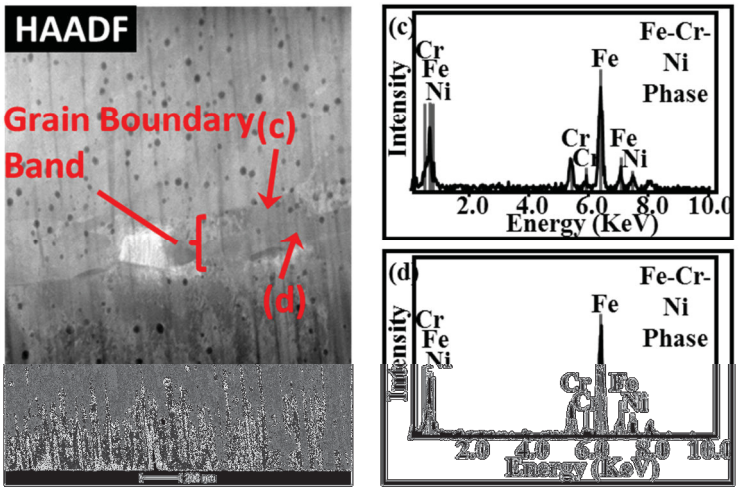

Location	Fe	Cr	Ni
	Wt.%		
(c)	74.5	19.7	6.6
(d)	82.5	12.9	4.6

Figure 24. TEM and composition analysis of the band ahead of Crack 2 from the 2% swelling specimen.

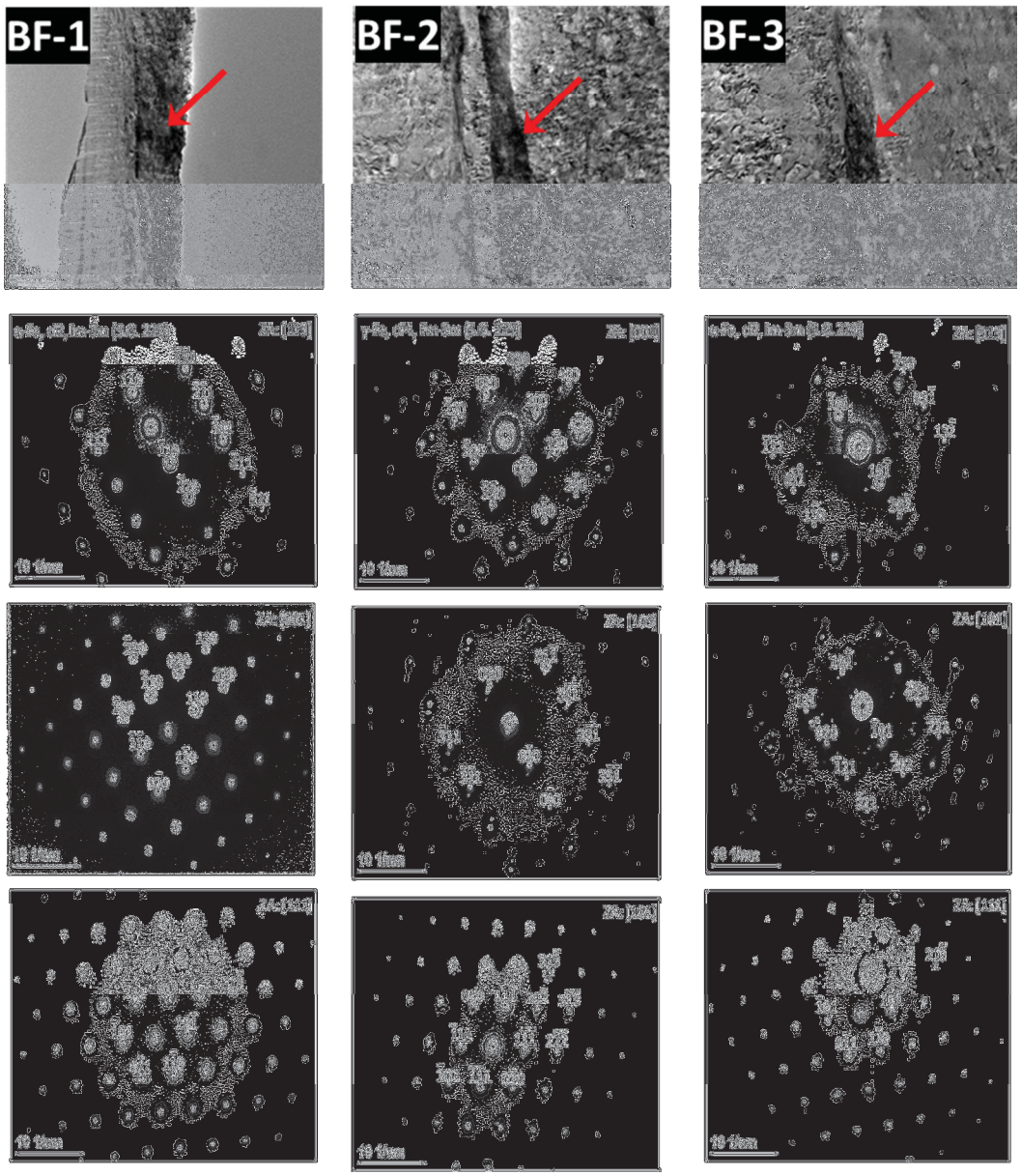

Figure 25. Diffraction analysis of the various components of the band ahead of Crack 2 from the 2% swelling specimen.

3.4 Grain Boundary Cohesion

At this writing, only the data generated with the material with 2% swelling were available. Specimens were machined either in the bulk material (monocrystal) to determine the material behavior or such that the specimen contained a single grain boundary to determine grain boundary cohesion. A total of six specimens were tested. None of the tests performed showed a failure at the grain boundary. Deformation was more pronounced on one side of the grain boundary than the other based on the respective grain orientation with regard to the tensile axis, and the specimens always failed by ductile fracture on one side of the grain boundary. Figure 26 shows Tensile Bar 5 before and after testing. Deformation clearly occurred in one grain of orientation $[16\bar{2}]$, and failure occurred in this grain. From the stress-strain curve generated, the yield strength was 892 MPa, and the CRSS was 418 MPa. Tensile Bar 6 was a single crystal of orientation $[\bar{2}\bar{3}2]$. The yield strength was 1,160 Mpa, and its CRSS was 400 MPa (Table 3).

For comparison, those values are similar to values measured from 304 stainless-steel specimens irradiated with protons to 10 dpa at a dose rate of ~8×10^{-6} dpa/s and a temperature of 360°C ± 10° by the Michigan Ion Beam Laboratory (Vo et al. 2017).

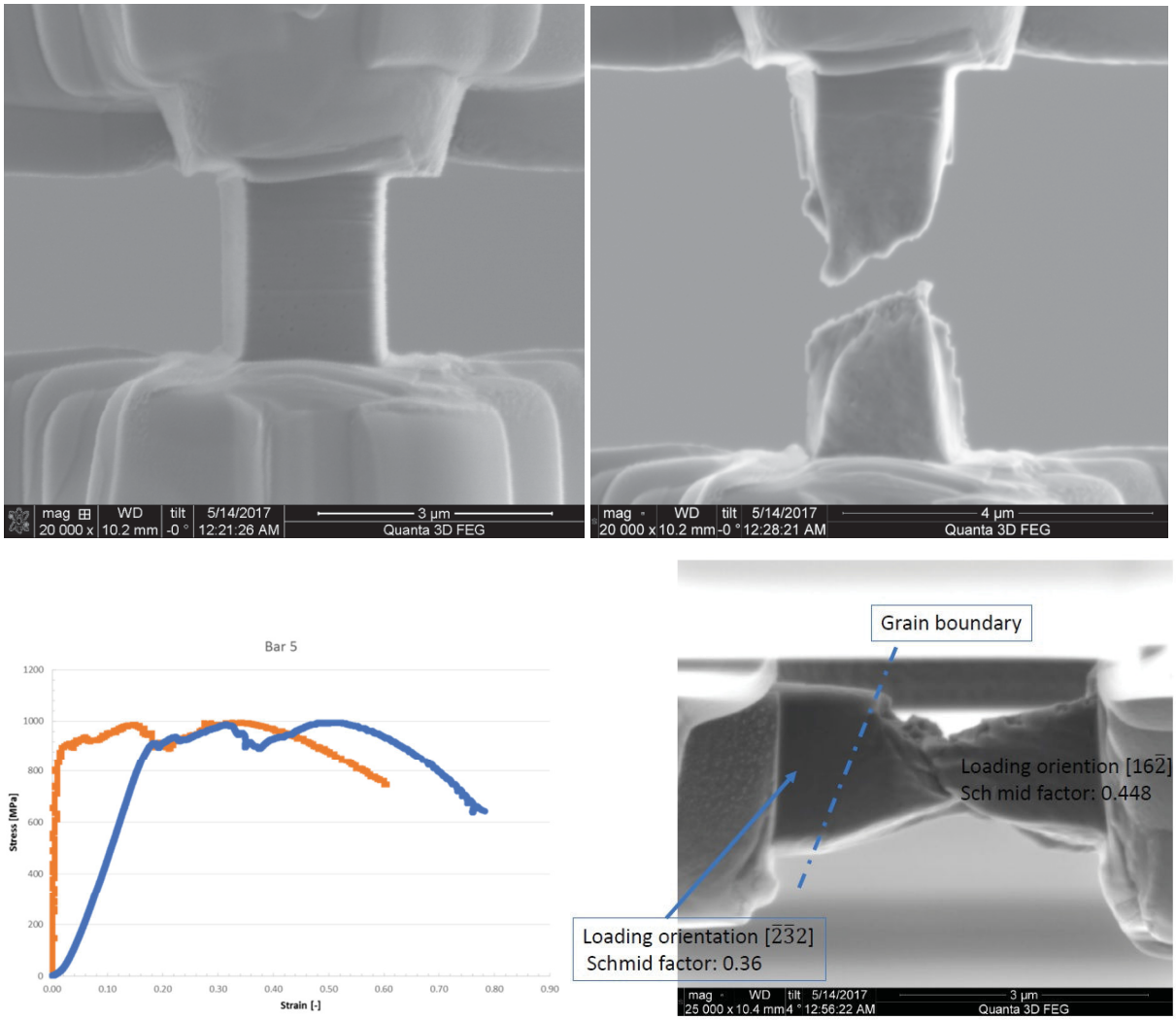

Figure 26. Tensile Bar 5 before and after tensile test.

Table 3. YS and CRSS determined from the 2% swelling specimen.

Tensile Bar No.	YS (MPa)	Loading Orientation	Schmid Factor	CRSS (MPa)
5	⍰892	[16$\bar{2}$]	0.448	⍰400
6	⍰1,160	[$\bar{2}\bar{3}$2]	0.36	⍰418

To increase the odds of measuring the cohesion of the grain boundary, notched specimens were used. Those specimens had a reduced cross section on the grain boundary area, and stress applied was higher on the grain boundary than on the surrounding matrix. An example is presented in Figure 27, which shows Tensile Bar 4 before testing, with the grain boundary aligned between the notches, and after failure where part of the fracture surface can be seen. He ion imaging of the fractured surface (Figure 28) shows that

Failure did not occur at the grain boundary despite the localization of the notches and deformation observed within the surrounding grain.

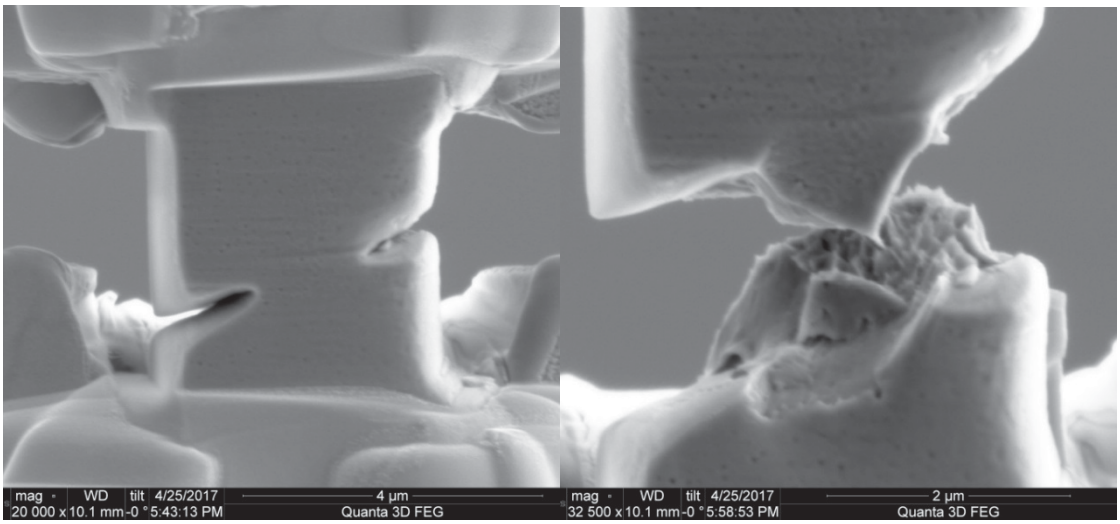

Figure 27. Notched Tensile Bar 4 before and after tensile test.

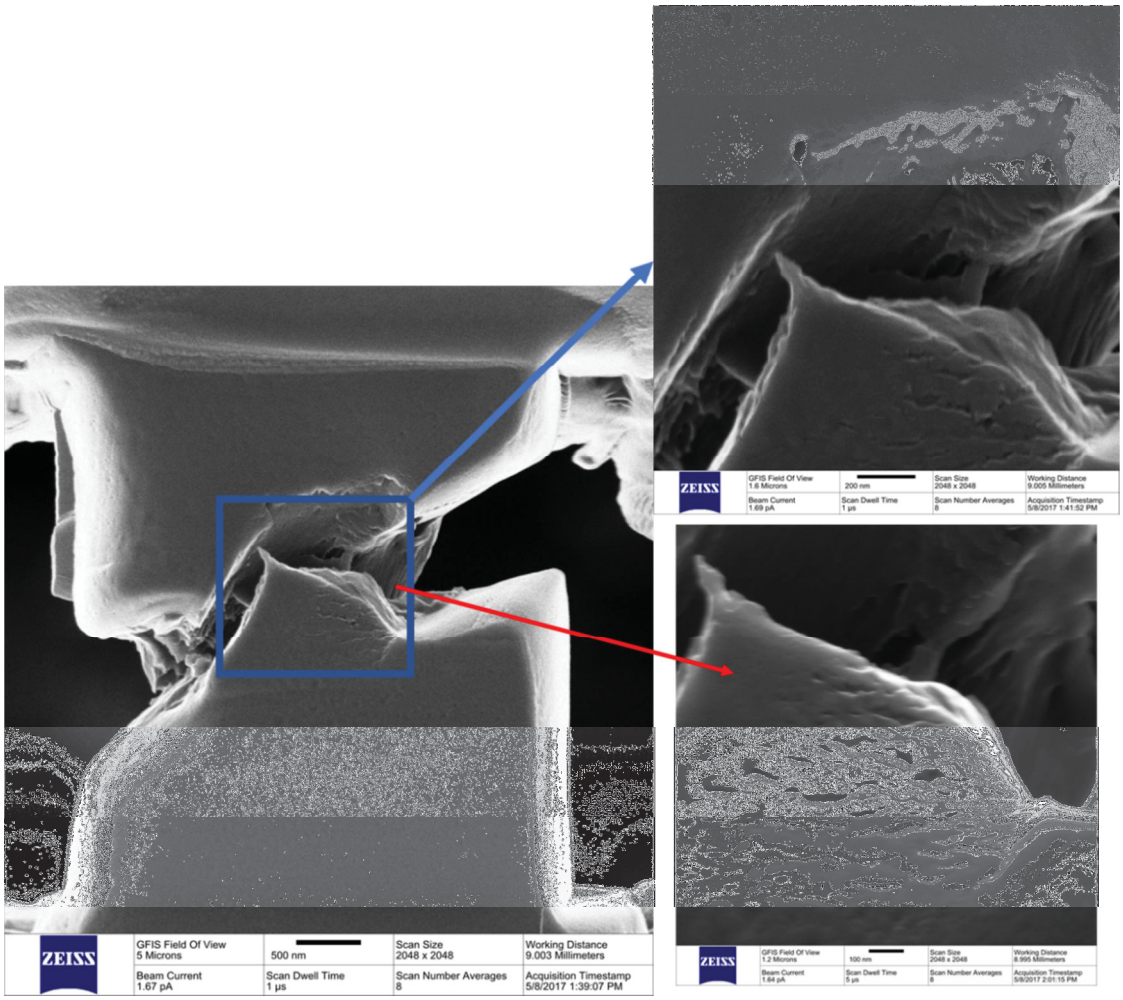

Figure 28. He ion imaging of Tensile Bar 4 after tensile test.

4. CONCLUSIONS

The effect of swelling on IASCC CGRs was investigated on 304 stainless-steel that had been irradiated to 27 dpa in Experimental Breeder Reactor II at Idaho National Laboratory. Two levels of swelling were investigated: 2 and 3.7%. IASCC experiments suggested that this material was much less susceptible to IASCC than materials irradiated under light water reactor conditions. Analysis of grain boundaries ahead of crack tips indicated the presence of "bands" that may be due to phase transformation. However, there is no evidence that such phases were a consequence of the propagation of the IASCC crack. It is likely that several grain boundaries are decorated with by such features and that those features may impede crack propagation. Micromechanical testing did not show any evidence that the grain boundaries were embrittled by the presence of voids, which is consistent with the observation that voids were present mainly inside grains and not at grain boundaries.

5. REFERENCES

Bond, G. M., et al., 1999, "Void swelling of annealed 304 stainless steel at ~370-385°C and PWR-relevant displacement rates," *9th International Conference on Environmental Degradation of Materials in Nuclear Power Systems – Water Reactors*, pp. 1045–1050.

Chopra, O. K. and A. S. Rao, 2011, "A review of irradiation effects on LWR core internal materials – IASCC susceptibility and crack growth rates of austenitic stainless steels," *Journal of Nuclear Materials*, Vol. 409, No. 3, pp. 235–256.

Garner, F. A. and B. J. Makenas, 2006, "Recent experimental results on neutron-induced void swelling of AISI 304 stainless steel concerning its interactive dependence on temperature and displacement rate," *Fontevraud-6 Symposium on Contribution of Materials Investigations to Improve the Safety and Performance of LWRs, Fontevraud, France, September 18–22, 2006*, pp. 625–636.

Garner, F. A., J. E. Flinn, M. M. Hall, and B. J. Makenas, 2007, "Recent insights on neutron-induced void swelling and irradiation creep of AISI 304 stainless steel," *Proceedings of 13th International Conference on Environmental Degradation of Materials in Nuclear Power Systems, Whistler, Canada, August 19–23*, 2007.

Garner, F. A., et al., 2013, "Void swelling and resultant strains in thick 304 stainless steel components in response to spatial gradients in neutron flux-spectra and irradiation temperature," *Proceedings of 16th International Conference on Environmental Degradation of Materials in Nuclear Power Systems, Asheville, North Carolina, August 11–15, 2013*.

Garner, F. A., et al., 2014, "Measurement of void swelling in thick non-uniformly irradiated 304 stainless steel blocks using nondestructive ultrasonic techniques," *Fontevraud-8 Symposium on Contribution of Materials Investigations and Operating Experience to LWRs' Safety, Performance and Reliability, Avignon, France, September 14–18, 2014*.

NUREG-0313, 1988, "Technical Report on Material Selection and Processing Guidelines for BWR Coolant Pressure Boundary Piping," Rev. 2, U.S. Nuclear Regulatory Commission, January 1988.

NUREG/CR-7027, 2010, "Degradation of LWR Core Internal Materials Due to Neutron Irradiation," U.S. Nuclear Regulatory Commission, December 2010.

Teysseyre, S., 2015, *Specimen Machining for the Study of the Effect of Swelling on CGR in PWR Environment*, INL/EXT-15-35594, June 2015.

Vo, H. et al., 2017, "In situ micro-tensile testing on proton beam-irradiated stainless steel," *Journal of Nuclear Materials*, Vol. 493, pp. 336–342.

Appendix A

Irradiation-Assisted Stress Corrosion Cracking Testing Facility

Appendix A

Irradiation-Assisted Stress Corrosion Cracking Testing Facility

The IASCC experiments were performed in a shielded testing loop. Water was continuously refreshed with a flow rate of about 200 mL/minute for a 4-L autoclave; the water chemistry was continuously monitored and controlled. The dissolved gas concentration was controlled by applying an overpressure of pure hydrogen at room temperature before water flowed into the high-pressure, high-temperature part of the loop. The ion content in the water was controlled by flowing water through an ion exchanger to remove corrosion products. The test was performed in a pressurized water reactor environment, meaning pure water with 1,000 ppm of boron and 2 ppm of lithium added and 25 cc/kg of dissolved hydrogen. Water chemistry was controlled by measuring water conductivity and pH. AT5 software provided by the GE Global Research Center was used to monitor crack growth control load. Crack length was monitored using the direct current potential drop technique.

For radiation protection, a support frame was installed around the autoclave. This frame offered a work space for specimen handling. The frame safely supported enough lead to provide shielding, with 4 in. of lead on the walls and 2 in. of lead plus 1 in. of steel on the floor (i.e., sample loading side). The frame was not in contact with the autoclave, which prevented heat transfer for the autoclave to the lead bricks. Each of the lead bricks had been powder coated to avoid any lead oxidation and any subsequent health hazard. A 1/8-in. steel cover protected the shield walls. The front of the cover can be lowered to provide access to the lead bricks that compose the front wall and the front wall can be partially removed to allow specimen loading and unloading.

Loading Procedure

The specimen was brought to the laboratory space in the testing facility shown in Figure A-1. The front of the shield was partially removed to allow operator access to transfer specimens. A guiding jig was placed in the autoclave for precise and quick loading of the specimens into the clevises (Figure A-2).

The bag containing the specimen was transferred from the yellow lead pig to the work area. The work area was equipped with a small storage niche that was available if there was a need to pause work. The can containing the specimen was removed from the plastic bag and opened. After verifying the specimen's identity, the specimen was loaded into the clevises and secured with the loading pin using long reach tongs. The guiding jig was then removed and the specimen was held in place by applying 50 lb. of load.

The next step consisted of welding the direct current potential drop leads to the short leads that were attached to the specimen (Figure A-3). After verifying the contact was strong enough and loading was satisfactory (Figure A-4), the autoclave body was lowered and the autoclave was sealed. The front shield was then put into place (Figure A-5).

After loading was complete, the radiation field was measured and posted. The dose rate in contact with the wall of the shield was 300 μR/hour, the dose rate just below the autoclave was 30 mR/hour, and the dose rate just above the autoclave was 29 mR/hour. The dose rate at the boundary of the restricted area was 15 μR/hour.

Water Chemistry Control

During the course of the experiment, water samples were taken weekly and analyzed for contamination; water chemistry was verified using ICP-OES. The sample is acidified with Optima nitric acid to a concentration of 1%. Analyses of lithium and boron were performed on the Thermo iCAP 6500

ICP-OES. Calibration and calibration checks were National Institute of Standards and Technology traceable standards in 1% trace metal nitric acid. A lithium two-point curve of 0 ppm and 10 ppm lithium and a boron two-point curve of 0 ppm and 1,002 ppm boron were generated prior to sample analysis. Calibration verification was performed using a 5-ppm lithium standard and a 100-ppm boron standard. The acceptable limit for calibration verification was ±10% for each analyte. The sample was diluted with 1% trace metal nitric acid to within the calibration range if it was outside the generated calibration curve.

Figure A-1. Laboratory prepared before reception of the specimen.

Figure A-2. Clevises and guiding jig prepared before loading the specimen.

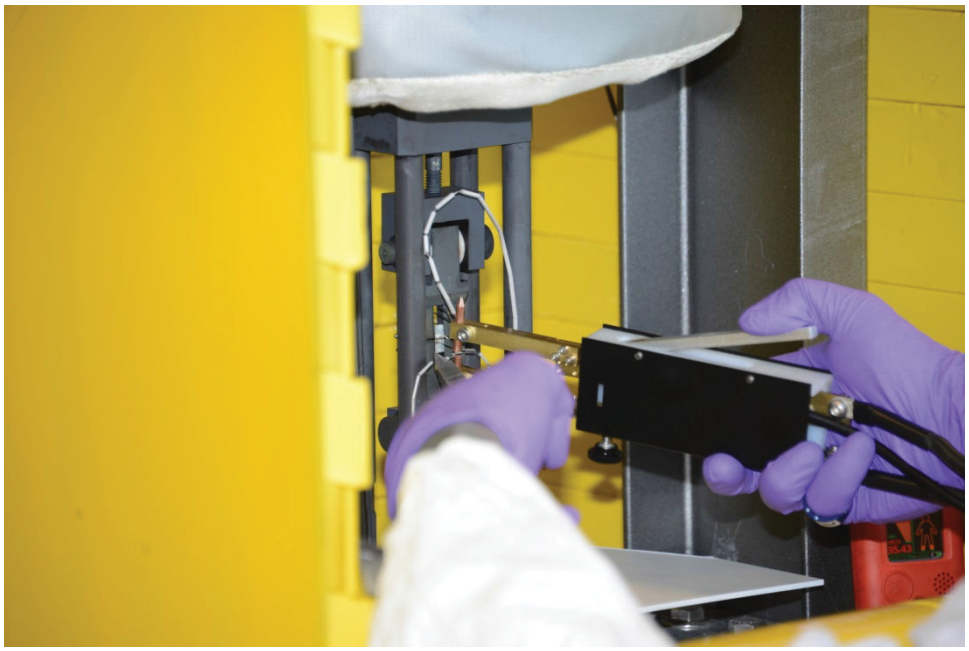

Figure A-3. The direct current potential drop leads being connected to the samples leads.

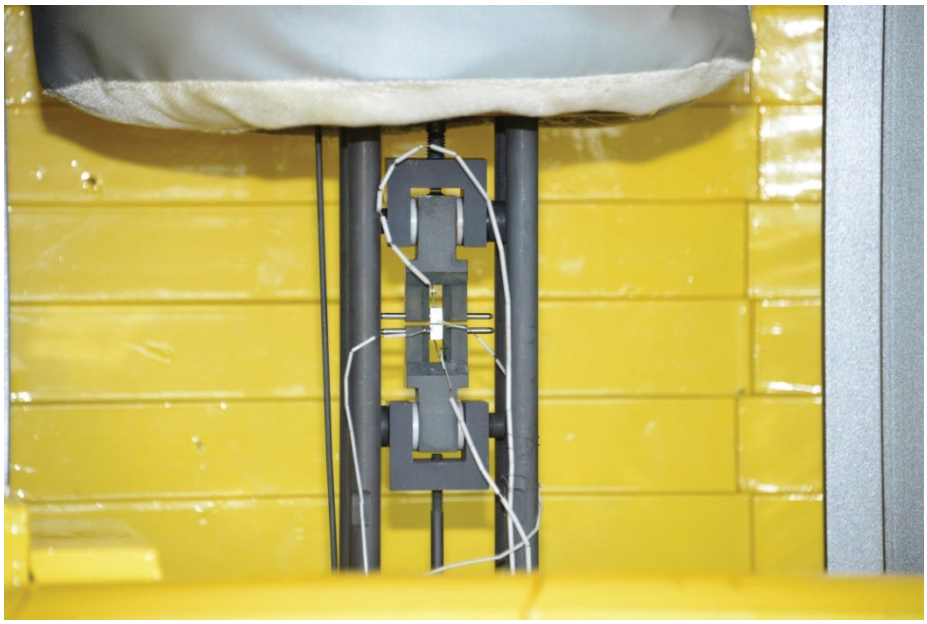

Figure A-4. Specimen loaded in the autoclave and ready to be tested.

Figure A-5. IASCC testing jig with shield closed.

Specimen Reception at the Testing Facility

To minimize the number of manipulations (e.g., cask loading, unloading, and storage), it was decided the specimens would be shipped on a demand basis. Only two CT specimens were shipped to the building where testing was performed; the remaining specimens were stored in another facility. Each specimen was shipped in an individual aluminum container, maintaining the specimen in place between foam inserts, as shown in Figure A-6. Each can was sealed in a plastic bag.

After receipt of the shipping cask at the facility, the plastic bags containing the specimens were transferred to a lead pig (Figure A-7). The lead pig was procured for this project by the facility where the experiments were performed. The inside dimensions of the lead pig are 4 in. in diameter by 12 in. high with the lid on the unit, and the walls, lid, and bottom of the lead pig are 2 in. thick. This container was used for specimen storage and transfer to the test jig.

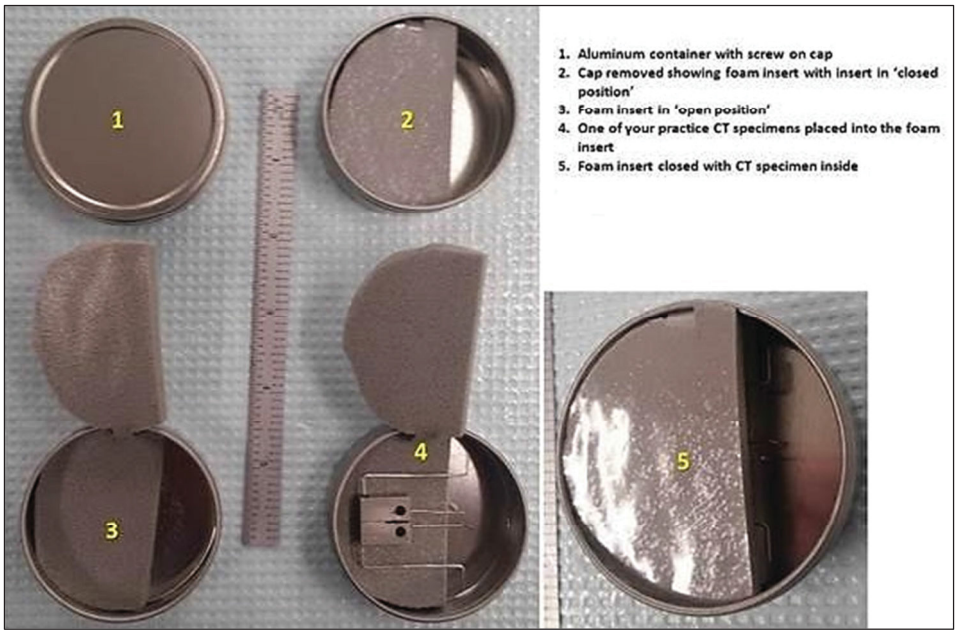

Figure A-6. Packaging of CT specimens with attached leads.

Figure A-7. The shipping container (in blue) contains the specimens. Those specimens will be transferred to the yellow lead pig for storage and transport within the testing facility.